Acoustic-Structure Interaction in an Adaptive Helmholtz Resonator by Compliance and Constraint

Shichao Cui
Department of Mechanical and Aerospace Engineering,
The Ohio State University,
Columbus, OH 43210
e-mail: cui.408@osu.edu

Ryan L. Harne[1]
Department of Mechanical and Aerospace Engineering,
The Ohio State University,
Columbus, OH 43210
e-mail: harne.3@osu.edu

The acoustic energy attenuation capabilities of traditional Helmholtz resonators are enhanced by various methods, including by coupled resonators, absorbing materials, or replacement of rigid walls with flexible structures. Drawing from these concepts to envision a new platform of adaptive Helmholtz resonator, this research studies an adaptive acoustic resonator with an internal compliant structural member. The interaction between the structure and acoustic domain is controlled by compression constraint. By applying uniaxial compression to the resonator, the flexible member may be buckled, which drastically tailors the acoustic-structure interaction mechanisms in the overall system. A phenomenological analytical model is formulated and experimentally validated to scrutinize these characteristics. It is found that the compression constraint may enhance damping capabilities of the resonator by adapting the acoustic-structure interaction between the resonator and the enclosure. The area ratio of the flexible member to the resonator opening and the ratio of the fundamental natural frequency of the flexible member to that of the enclosure are discovered to have a significant influence on the system behavior. These results reveal new avenues for acoustic resonator concepts exploiting compliant internal structures to tailor acoustic energy attenuation properties. [DOI: 10.1115/1.4045456]

Keywords: adaptive Helmholtz resonator, acoustic wave attenuation, elastic buckling, damping, structural acoustics, vibration control, vibration isolation

1 Introduction

The traditional Helmholtz resonator is a rigid-walled cavity with an open neck. At frequencies for which the acoustic wavelength is much longer than the cavity dimensions, a lumped parameter acoustic system is realized via the lumped acoustic spring in the cavity and the lumped air mass in the neck. Traditional Helmholtz resonators are commonly used for narrowband sound absorption [1,2]. Researchers have studied ways to broaden the effectiveness of such resonators for greater robustness in acoustic wave absorption capabilities. Helmholtz resonators with flexible characteristics have also been investigated [3–9]. Tang and Sirignano [10] studied resonator dimensions for enhanced damping and absorption. Selamet et al. [11] found that a lining on the rigid wall cavity may enhance dissipative influences and lower the resonant frequency.

Using multiple resonators may also improve the acoustic wave absorption. For instance, the acoustic coupling between an enclosure and a Helmholtz resonator array has been studied by Li and Cheng [12] through a model that enlightens optimal design. Zhao and Morgans [13] investigated suppressing two unstable modes in a combustion system by individual Helmholtz resonators with passive control of the neck opening areas. Griffin et al. [14] studied how two Helmholtz resonators mechanically coupled together can increase the transmission loss. Tang et al. [15] found that separating the cavity into compartments may result in additional resonances to broaden the frequency bandwidth of wave attenuation.

The use of flexible structures inside Helmholtz resonators may also introduce opportunities to exploit multi-degrees-of-freedom system dynamics for enhanced acoustic wave absorption. Kurdi et al. [16] and Nudehi et al. [3] replaced a wall of a cylindrical Helmholtz resonator cavity with a flexible end plate so that greater transmission loss may be achieved. Similarly, the noise reduction by a rectangular enclosure with a flexible wall is studied by Lyon [17] in terms of the stiffness influence of the enclosure and the flexible wall. Researchers have also investigated flexible structures utilized inside the cavity of the resonator, such as the coupled flexible panel and Helmholtz resonator studied by Sanada and Tanaka [4]. In the work [4], the flexible panel constitutes another degree-of-freedom that may broaden the working frequency range and enhance acoustic energy absorption capability via the coupling between acoustic and elastic physics.

For the flexible structure in the Helmholtz resonator, to more greatly couple the structural dynamics with the acoustic pressure changes, the structure must be highly slender [3,4]. Slender structures are often susceptible to buckling-based phenomena when utilized in confined dimensions of structural systems. Such susceptibility is of recent interest in the development of adaptive structures and materials [18,19]. For instance, Wang et al. [20] investigated utilizing the large elastic buckling of elastomeric beams to control the response of locally resonant acoustic metamaterials. The buckling of a slender beam can induce nonlinear, geometric deformations [21], so that the combination of nonlinear deformation, the criticality of buckling, and material properties may influence the behavior of the material system. In recent work by Cui and Harne [22], buckling of slender structures in a soft material system is found to dramatically tune the force transmission through the system. These representative results suggest that exploitation of elastic buckling of flexible, slender structures offers great opportunity to tune structural and material system properties. Many of the Helmholtz resonators reported in the literature use rigid materials to fabricate the resonator cavity, although rigid materials may not be suitable for all applications. In fact, elastomeric structures like those of growing, recent interest [18–23], are commonly required in engineering applications for vibration, shock, and noise suppression purposes. On the other hand, the use of such materials to enable adaptive control over acoustic-elastic properties of a Helmholtz resonator via controlled elastic buckling phenomena has yet to be explored.

[1]Corresponding author.

Contributed by the Noise Control and Acoustics Division of ASME for publication in the Journal of Vibration and Acoustics. Manuscript received August 27, 2019; final manuscript received November 4, 2019; published online November 12, 2019. Assoc. Editor: Stefano Lenci.

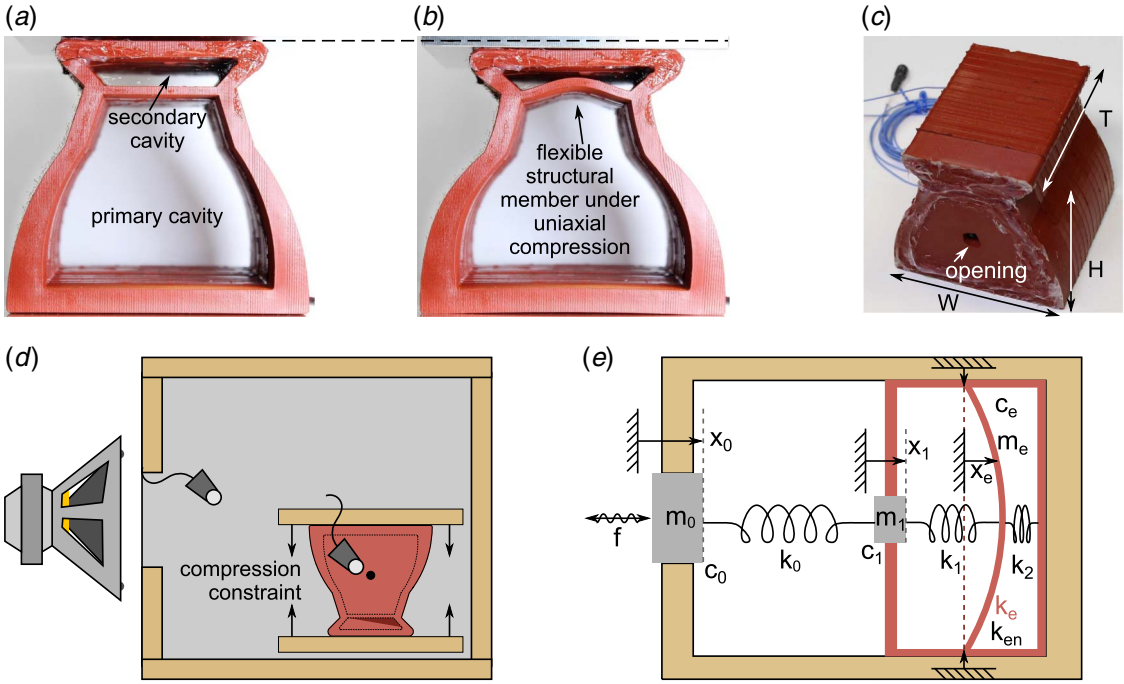

Fig. 1 (*a*) Cross-section of the Helmholtz resonator. Below the horizontal flexible structural member is the primary cavity, and above is the secondary cavity. (*b*) Compressed configuration of the Helmholtz resonator cross section. (*c*) Complete resonator geometry and dimensions. (*d*) Schematic for acoustic experimental setup. (*e*) Schematic of the lumped parameter model of the experimental setup in (*d*).

This study investigates the potential to leverage a flexible, buckling structural member within an adaptive Helmholtz resonator. The investigation of the flexibility and acoustic-structure interaction may open up new ways for the resonator design. This report is organized as follows. First, the composition and fabrication of a proof-of-concept resonator designed with such a vision are introduced. Then, a lumped parameter phenomenological analytical model is proposed to characterize the essential acoustic-structure interaction mechanisms and resulting acoustic energy attention capability of the resonator when deployed with a host acoustic enclosure. A finite element (FE) model is developed to characterize the deformation of the resonator under compression constraint so as to bridge the analytical model to the experiment. Following experimental validation, the model is harnessed to gain fundamental knowledge on the key acoustic-structure interactions between the Helmholtz resonator with flexible members and the host acoustic enclosure to explore practical opportunities of leveraging such system for acoustic wave control. Finally, conclusions and discussions are provided to summarize the knowledge gained and practical outlooks.

2 Adaptive Helmholtz Resonator Composition and Experimental Setup

To investigate leveraging acoustic-structure interaction in an adaptive Helmholtz resonator with an internal flexible structural member, a proof-of-concept experimental resonator is fabricated. The cross-section of the Helmholtz resonator is shown in Fig. 1(*a*). The cross-sectional structure consists of an outer shell-like geometry where the thinnest and the thickest part are 0.005 m and 0.01 m thick, respectively. A slender structural member with thickness 0.003 m divides the cross-section into two cavities. When subjected to a uniaxial compression in the vertical direction, the deformation of the outer shell results in compression of the slender member which may buckle as shown in Fig. 1(*b*). Since a Helmholtz resonator requires a closed volume with an opening, the cross-section ends are finished with wall-like pieces seen in Fig. 1(*c*). When the cross-section ends are sealed with the end walls, the buckling of the flexible member under compression is not as dramatic as that shown in Fig. 1(*b*) so that the primary and secondary cavity volumes are not as greatly changed. The completed, proof-of-concept adaptive Helmholtz resonator is shown in Fig. 1(*c*). The total width is $W = 0.1$ m, total height is $H = 0.09$ m, and total thickness is $T = 0.09$ m.

To fabricate the resonator, silicone rubber (Smooth-on, Inc., Mold Max 60) is poured into a mold negative and cured at room temperature for sufficient time. An opening is made by incision into the silicone rubber material to form the neck of the Helmholtz resonator, as indicated in Fig. 1(*c*). Refined tuning of the opening radius is achieved by inserting dense modeling clay around the opening perimeter. The bulk silicone rubber used for fabrication has material properties: Young's modulus 2.2 MPa, Poisson's ratio 0.49, and density 2100 kg/m^3. The primary cavity, Fig. 1(*a*), which constitutes the resonating volume of the Helmholtz resonator occupies a volume of 3.07×10^{-6} m^3.

To examine the sound attenuation capabilities of the resonator and influences of the compression of the flexible structural member within, acoustic experiments are conducted. The experimental setup schematic is presented in Fig. 1(*d*). The resonator is placed inside an enclosure made of medium density fiberboard of thickness 0.019 m. The enclosure has a cubic cavity of side length 0.254 m, which results in a total volume of 0.0164 m^3. The opening of the enclosure is a square of side length 0.1524 m. The cavity and opening of the enclosure result in a Helmholtz resonance of the enclosure around 164 Hz, which is the target frequency for attenuation when the dimensions of the resonator are considered. The enclosure introduces an acoustic domain with which the adaptive Helmholtz resonator interacts. Here, the acoustic-structure interaction among the enclosure-resonator-flexible member system is investigated. In this study, the Helmholtz resonator absorbs acoustic energy in a way analogous to resonant elastic metamaterials [24], where the motion of the metamaterial masses is 90-deg out-of-phase with the motion of an input vibration source.

For purposes of applying compression constraints to the resonator, the adaptive Helmholtz resonator is placed between two pieces of medium density fiberboard whose distance apart is adjusted by

threaded rods and nuts. A loudspeaker is mounted on one side of the enclosure to excite the enclosure. Two microphones (PCB 130E20) are used to measure the acoustic pressure. One microphone is inserted into the enclosure cavity and hung at a location that is slightly off-center. The second microphone is inserted into the primary cavity of the resonator via a separate opening that is sealed up after the microphone is inserted. In this way, the Helmholtz resonator has just one working opening to couple the primary cavity volume to the enclosure volume via the designed neck opening, as shown in Figs. 1(*c*) and 1(*d*). Sine sweep signals from 50 to 250 Hz are used to drive the loudspeaker and thus excite acoustic pressure variations in the enclosure.

3 Analytical Modeling of the Adaptive Helmholtz Resonator and Enclosure System

A lumped parameter model is devised to analytically study the dynamic behavior of the resonator and enclosure system. The schematic of the model is shown in Fig. 1(*e*). Based on the Helmholtz resonance of the enclosure around 164 Hz and the attention of this research to such low-frequency range respecting the size of the enclosure and resonator, the long-wavelength approximation is taken to characterize the acoustic-elastic system via lumped parameter equivalents. The air in the opening of the enclosure, the air in the opening of the resonator, and the lowest-order modal mass of the flexible structural member are thus considered to be lumped masses. Similarly, the compressibility of the air in the cavity of the enclosure and of the air in the cavities of the resonator is considered to be lumped springs. The analytical model is phenomenological in the sense that qualitative agreement is sought for approximation of the system behaviors. In the model, only the lowest order mode of vibration is considered for the flexible member due to frequency range interested.

For the enclosure opening, the acoustic mass is $m_0 = \rho_0 S_0 t_0^*$, where ρ_0 is the density of air, $S_0 = \pi a_0^2$ is the opening area, and a_0 is the characteristic opening radius. The dimension $t_0^* = t_0 + 1.7a_0$ is the thickness of the opening t_0, including the end correction for the flanged opening [2,25]. The equation of motion for the air mass m_0 having displacement x_0 is then obtained by consideration of dynamic equilibrium

$$\rho_0 S_0 t_0^* \ddot{x}_0 = -c^2 \rho_0^2 S_0 dv_0 \tag{1}$$

where c is the sound speed in air and dv_0 is the differential specific volume change. Xu et al. [26] report that the differential specific volume change is expressed as

$$dv_0 = \frac{S_0 x_0 - S_1 x_1}{\rho_0 V_0} \tag{2}$$

Here, $S_1 = \pi a_1^2$ is the area of the opening in the adaptive resonator, x_1 is the displacement of the acoustic mass in the resonator opening, a_1 is the characteristic opening radius of the resonator, and V_0 is the volume of the enclosure cavity. By substituting Eq. (2) into Eq. (1) and rearranging terms, the undamped and unforced governing equation of motion for the air mass m_0 is

$$\ddot{x}_0 + \frac{c^2 S_0}{V_0 t_0^*} x_0 - \frac{c^2 S_1}{V_0 t_0^*} x_1 = 0 \tag{3}$$

Considering the harmonic pressure excitation shown in Fig. 1(*e*) and the loss factor η_0 due to air flow resistance through the enclosure opening, the governing equation is written as

$$\ddot{x}_0 + \eta_0 \omega_0 \dot{x}_0 + \frac{c^2 S_0}{V_0 t_0^*} x_0 - \frac{c^2 S_1}{V_0 t_0^*} x_1 = \frac{P_0}{\rho_0 S_0 t_0^*} S_0 \cos \Omega t \tag{4}$$

The natural frequency of the enclosure without the resonator is $\omega_0 = \sqrt{c^2 S_0 / (V_0 t_0^*)}$.

The acoustic mass in the adaptive Helmholtz resonator opening is $m_1 = \rho_0 S_1 t_1^*$, where $t_1^* = t_1 + 1.7a_1$ is the end-corrected opening thickness of the actual resonator wall thickness t_1. By considering the dynamic equilibrium of the displacement x_1 of the air mass m_1, the governing equation is obtained

$$\rho_0 S_1 t_1^* \ddot{x}_1 = -c^2 \rho_0^2 S_1 dv_1 + c^2 \rho_0^2 S_1 dv_0 \tag{5}$$

where

$$dv_1 = \frac{S_1 x_1 - S_2 x_e}{\rho_0 V_1} \tag{6}$$

Here, V_1 is the volume of the primary cavity of the resonator, S_2 is the area of the flexible structural member that interfaces with V_1, and x_e denotes the displacement of the flexible member. Substituting Eq. (6) into Eq. (5) and rearranging terms yield the governing equation of motion for the air mass m_1 in the resonator neck

$$\ddot{x}_1 + \eta_1 \omega_1 \dot{x}_1 + \left[\frac{c^2 S_1}{V_1 t_1^*} + \frac{c^2 S_1}{V_0 t_1^*}\right] x_1 - \frac{c^2 S_2}{V_1 t_1^*} x_e - \frac{c^2 S_0}{V_0 t_1^*} x_0 = 0 \tag{7}$$

The loss factor η_1 is introduced to account for air flow resistance through the resonator opening. The fundamental natural frequency of the resonator opening and primary cavity is $\omega_1 = \sqrt{c^2 S_1 / (V_1 t_1^*)}$.

Finally, the governing equation of motion for the lowest-order generalized displacement of the flexible structural member x_e is obtained

$$m_e \ddot{x}_e = -k_e (1 - p) x_e - k_{en} x_e^3 + c^2 \rho_0^2 S_2 dv_1 - c^2 \rho_0^2 S_2 dv_2 \tag{8}$$

Here, $m_e = \zeta M_e$ is the mass contribution to the lowest-order vibration of the flexible member. The mass contribution m_e is a portion ζ [27,28] of the total mass $M_e = \rho_e V_e$ of the flexible member, which is determined by the density ρ_e and volume V_e of the flexible member. The fundamental elastic stiffness k_e of the flexible member is defined as $k_e = m_e \omega_e^2$, where ω_e is the lowest-order natural frequency of the flexible panel. According to a study of rectangular plates by Leissa [29], the lowest order natural frequency of a rectangular panel can be approximated from a vibration frequency factor λ that is expressed as

$$\lambda = \omega_e a^2 \sqrt{\rho_e / D} \tag{9}$$

A tabulated set of frequency factors λ is available based on the panel aspect ratio a/b [29]. Equation (9) is the vibration frequency factor for flexible panels that are simply supported on two opposite sides of length a, and clamped on the other two opposite sides of length b. These are similar to the boundary conditions of the flexible structural member used in this work. In Eq. (9), $D = Eh^3/[12(1 - \nu^2)]$ is the bending stiffness determined by the isotropic Young's modulus E, Poisson's ratio ν, and thickness h of the flexible member.

In Eq. (8), the flexible member is subjected to axial compression constraint characterized by the load parameter p, as a proportion of the fundamental Euler buckling load. Nonlinear geometric deformation is subsequently included since elastic buckling may be manifest. With a thickness to length ratio of less than 0.1 in each direction for the flexible member, the member is considered sufficiently thin to neglect span-wise modal coupling in this low-frequency range. As a result, a nonlinear force determined by the product of a stiffness k_{en}, which is proportional to the elastic stiffness k_e by coefficient β Eq. (A1*c*), and the cubic power of displacement x_e is introduced [30]. Here, dv_2 is given by

$$dv_2 = S_2 x_e / (\rho_0 V_2) \tag{10}$$

where V_2 is the secondary volume of the resonator. Substituting Eq. (10) into Eq. (8) and rearranging terms yields the governing

equation of motion for the mass m_e

$$\ddot{x}_e + \eta_e \omega_e \dot{x}_e + \left[\omega_e^2(1-p) + \frac{c^2\rho_0 S_2^2}{V_2 m_e} + \frac{c^2\rho_0 S_2^2}{V_1 m_e}\right] x_e + \frac{k_{en}}{m_e} x_e^3 - \frac{c^2\rho_0 S_1 S_2}{V_1 m_e} x_1 = 0 \tag{11}$$

The elastic loss factor η_e is introduced to account for hysteretic damping in the flexible member. Because the lowest-order dynamics are considered for the flexible member, the damping model may be empirically identified, and as such the elastic loss factor is used without loss of generality.

The governing equations for the three degree-of-freedom acoustic-elastic systems are (4), (7), and (11). Then, the harmonic balance method [31] is utilized to approximately solve for the steady-state dynamic response. The detailed steps for solving the governing equations are given in the Appendix.

In addition to the air mass displacements and flexible member generalized displacement, the complex-valued transfer function of the acoustic pressure inside the primary cavity of the resonator to the acoustic pressure inside the enclosure cavity of the enclosure is computed. The amplitude H and phase Φ, Eq. (A12), of the transfer function are used to explore the acoustic-structure interaction phenomena. To assess the effectiveness of the resonator to suppress the acoustic energy in the enclosure, the sound pressure level (SPL), Eq. (A11), is computed using the acoustic pressure in the enclosure.

4 Finite Element Modeling of the Adaptive Helmholtz Resonator

In order to relate the compression constraint applied in the experiments to the load parameter p in the analytical model, a FE model in ABAQUS CAE is developed. Figure 2(*a*) is the schematic of the 3D model of the resonator developed in ABAQUS using the exact geometry of the fabricated resonator. An isotropic, Neo-Hookean, hyperelastic material model is applied to characterize the resonator using the material properties given in Table 1. The bottom of the resonator is fixed, and the compression is applied to the top surface of the resonator in the vertical direction shown in Fig. 2(*a*) using a dynamic-implicit formulation. Presented in Fig. 2(*b*) is the deformation of the resonator without front face under 5.6% engineering strain colored according to the von Mises stress. The volumetric change of the primary resonator cavity is less than 1% of the cavity in the absence of the flexible member deformation. The engineering strain ε is the ratio of the applied compressive displacement to the total height H of the resonator. By removing the front face of the resonator from view in Fig. 2(*b*), the deformation and stress over the flexible member are apparent.

Table 1 Parameters for analytical modeling

ρ_0 (kg/m^3)	c (m/s)	a_0 (m)	t_0 (m)	V_0 (m^3)	a_1 (mm)	t_1 (m)
1.2	343	0.0874	0.019	0.01639	4.7/4.2/3.8	0.007
V_1 (m^3)	E (N/m^2)	h (m)	ν	ζ	V_2 (m^3)	η_0
0.000307	2.2e6	0.003	0.49	0.1	2.68e−5	0.05
η_1	η_e	β	F_0	ρ_e (kg/m^3)	V_e (m^3)	S_2 (m^2)
0.15	0.05	0.1	0.0006	2100	8.04e−6	0.00268

The FE results of engineering strain von Mises stress are presented in Fig. 2(*c*). The stress is measured from the middle point of the flexible member edge on the left, at the evaluation point shown in Fig. 2(*b*). The critical point is defined at 7.78% strain where the slope of the curve in Fig. 2(*c*) approaches zero, as indicated by the marker and legend in Fig. 2(*c*). Analytically, the critical value of the load parameter p^* is the value that makes the coefficient of x_e in the governing equation Eq. (11) equal zero. The critical value p^* is obtained by solution to Eq. (12).

$$\omega_e^2(1-p^*) + \frac{c^2\rho_0 S_2^2}{V_2 m_e} + \frac{c^2\rho_0 S_2^2}{V_1 m_e} = 0 \tag{12}$$

Using the parameters in Table 1, the critical load for the resonator is $p^* = 1.75$. Assuming that a null load parameter corresponds to zero strain and that $p^* = 1.75$ corresponds to $\varepsilon = 7.78\%$, then the linear relationship between the load parameter p and engineering strain ε is Eq. (13).

$$p = 0.225\varepsilon \tag{13}$$

The relationship of Eq. (13) is used to relate analytical model results with load parameters to the corresponding experimental measurements of engineering strains. The load parameters corresponding to the specific engineering strains are presented in Fig. 2(*c*) on the bottom x-axis label. The correlation between the engineering strains applied in the experiments and the load parameters in the analytical model results in Sec. 5 adopts the relationship obtained here through the finite element study.

5 Experimental Validation of the Analytical Model

An experimental validation of the analytical model is undertaken to establish confidence in the capability of the lumped parameter modeling approach. For the low-frequency range interested in this study, the wavelength is much longer than the dimensions of the enclosure and the resonator. Thus, the pressures inside the enclosure and inside the resonator are uniform. Therefore, the point microphone measurements inside the cavities accurately represent the system dynamics. Physical parameters from the

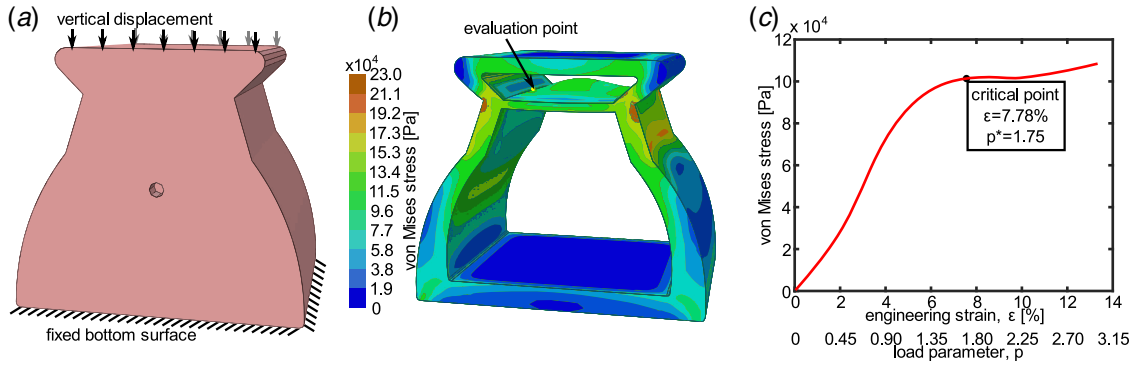

Fig. 2 (*a*) Schematic of a finite element model of the uncompressed HR. (*b*) FE results of the cross-section when the complete HR is under 5.6% engineering strain. Color shading indicates the von Mises stress. (c) FE results of engineering strain von Mises stress. The relationship between load parameter and strain is indicated in *x* labels, and the critical point is indicated by the legend.

enclosure-resonator system used in experiments that are subsequently employed in model calculations are listed in Table 1. Parameters included in Table 1 that are not introduced in the derivation in Sec. 3 are defined in the Appendix. The resonant frequency of the enclosure is 164 Hz, and remains unchanged in the study. For the analytical results, the parameter $\lambda = 14,\ 538$ is used. This parameter is selected since the boundary conditions of the flexible structural member are not precisely the same as those idealized in Ref. [29]. The damping terms η_0, η_1, and η_e, excitation F_0, and nonlinear to linear stiffness ratio of the resonator β, are identified empirically.

5.1 Controlling Enclosure Sound Pressure Level by Helmholtz Resonator Design and Constraint. A comparison between experimental and analytical results of the SPL inside the enclosure is presented in Fig. 3. The experimental results of the enclosure SPL are obtained from the microphone inside the enclosure, labeled as M1 in Fig. 1(*d*). In Figs. 3(*a*)–3(*c*), the experimental results are shown for three opening radii, 4.5 mm, 3.5 mm, and 2.5 mm. The baseline (thin solid curves) is the experimental result of the enclosure SPL without the resonator inside the enclosure cavity. A rigid mass occupying the same volume as the resonator is placed in the enclosure cavity during baseline experiments. For experimental results that introduce the resonator into the enclosure, the compression constraint achieved by the experimental fixture is specified in engineering strain ε as indicated in the legends. In Figs. 3(*d*)–3(*f*), the analytical results of SPL are shown for three opening radii, 4.7 mm, 4.2 mm, and 3.8 mm. The baseline (thin solid curves) is the response of the enclosure without a resonator, and the other curves correspond to the SPL with the addition of the resonator. For each opening radius, results considering the uncompressed condition $p = 0$ (thick solid curves) and two compressed conditions of specific load parameters related to the experimental engineering strains are presented.

The influence of change in the opening radius for the resonator is examined by comparing the results of the columns in Fig. 3. Experimentally, from Figs. 3(*a*)–3(*c*), the attenuation of the resonator is first quantified by comparing the SPL reduction of the uncompressed condition (0% engineering strain ε) to the baseline. For Figs. 3(*a*)–3(*c*), the opening radii are 4.5 mm, 3.5 mm, and 2.5 mm, the frequency ranges of SPL reduction are 165–214 Hz, 163–200 Hz, and 164–192 Hz, and the SPL reductions at 175 Hz are 1.85 dB, 3.86 dB, and 3.14 dB, respectively. When the opening radius decreases, the effective frequency range is narrowed, yet the SPL reduction is increased. The analytical results presented in Figs. 3(*d*)–3(*f*) show similar influences as those in the experiments. In the analysis, for the uncompressed condition $p = 0$ the three opening radii are 4.7 mm, 4.2 mm, and 3.8 mm. In experiments, the material and structural compliance of the Helmholtz resonator softens the equivalent stiffness of the resonator, and thus greater radii than experimental results are adopted in analytical study to compensate for the compliance. It is seen from analysis that the reduction in opening radius leads to narrower frequency ranges wherein the SPL is reduced from the baseline level. Specifically, the effective frequency ranges for Figs. 3(*d*)–3(*f*) are 160–214 Hz, 159–199 Hz, and 157–186 Hz, respectively. In addition, the SPL reductions in Figs. 3(*d*)–3(*f*) at 175 Hz are 2.6 dB, 3.6 dB, and 4.34 dB, respectively. The peak SPL reduction trends are in qualitative agreement with the experimental findings.

By increasing or decreasing the opening radius of the resonator, the natural frequency of the resonator is changed. Specifically, the smaller opening radius decreases the natural frequency of the resonator and brings it closer to the resonant frequency of the enclosure. Consequently, the maximum SPL reduction is enhanced although the frequency range of effective SPL reduction may be slightly reduced. For traditional Helmholtz resonators, reducing the opening radius may lead to a reduction in the magnitude of acoustic wave absorption due to reduction in acoustic mass in the resonator neck and increase in air flow resistance [25]. Yet, in this research

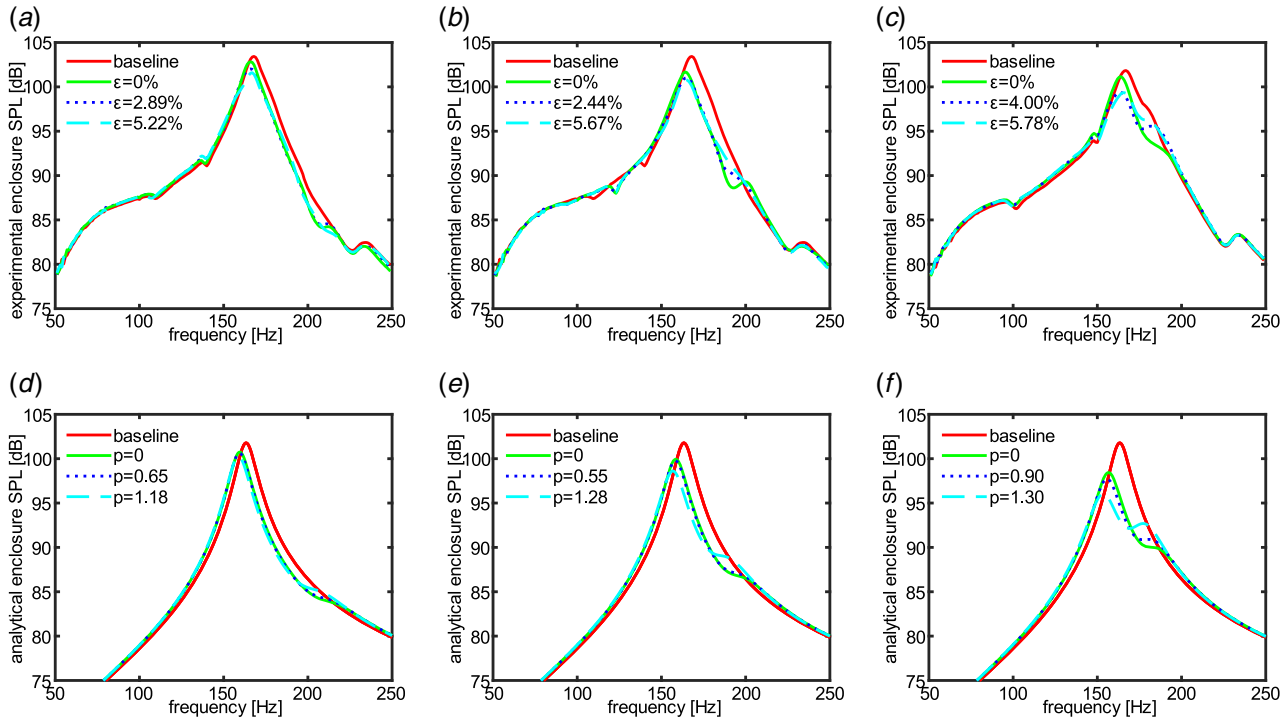

Fig. 3 Experimental results for enclosure SPL of different resonator opening radii (*a*) 4.5 mm, (*b*) 3.5 mm, and (c) 2.5 mm. Thin solid curves are the baselines (enclosure only) for each set of experiments. The applied compression, engineering pre-strain ε, for each experiment is specified in the legends. Analytical results for enclosure SPL of opening radius (*d*) 4.7 mm, (e) 4.2 mm, and (*f*) 3.8 mm, where thin curves are the baselines, thick curves are the uncompressed conditions, $p = 0$, and dotted and dashed curves are the compressed conditions of load parameters indicated in the legends.

reducing the opening radius of the adaptive Helmholtz resonator increases the SPL reduction and hence increases the wave absorption by the resonator. This may be due to the fact that a smaller resonator opening radius results in a greater area ratio of the flexible member to the resonator opening $\delta_2 = S_2/S_1$. For instance, the δ_2 values for Figs. 3(*d*)–3(*f*) are 38.62, 48.36, and 59.08, respectively. A greater area ratio δ_2 would more strongly couple the acoustic air in the resonator primary cavity to the structural dynamics of the flexible member. This stronger coupling may explain the enhancement of the SPL reduction in the enclosure achieved by smaller opening radii. Yet, it must be noticed that the opening area needs to be great enough to maintain the air flow through the opening.

After examining the influence of the opening radius of the resonator, the effect of the compression constraint applied to the resonator is contrasted between analytical and experimental trends. Tuning the compression constraint modulates the peak SPL value. Experimentally in Fig. 3(*c*), for $\varepsilon = 0\%$ the highest SPL is near 164 Hz, and by applying compression to $\varepsilon = 4.00\%$ and then to $\varepsilon = 5.78\%$, the SPL reduces at this peak value. In addition, at higher frequencies, for instance around 180 Hz in Fig. 3(*c*), with the increase of ε the SPL in the enclosure increases. The analytical results reveal similar physical behavior by the increase in load parameter p. For instance in Fig. 3(*f*) comparing the uncompressed condition $p = 0$ to the compressed conditions $p = 0.90$ and $p = 1.30$, as p increases, the SPL at 157 Hz decreases, while the SPL at 180 Hz increases. This effect is similar to that increased damping on a traditional mass-spring-damper resonator has on the vibration of a host structure [32]. In other words, the increase in damping for a mass-spring-damper increases the host structure response amplitude at the tuned frequency while also lowering the resultant peaks of modal response created by the two degrees-of-freedom system. Such enhancement of damping by increased compression applied to the resonator is further observed for the other cases presented in Figs. 3(*a*), 3(*b*), 3(*d*), and 3(*e*). The agreement of qualitative behavior between analysis and experiment enables the conclusion that the change of opening radius primarily tailors the frequency of the resonant phenomena whereas adjusting the compression constraint applied to the adaptive Helmholtz resonator tunes the damping. Lakes [33] found that buckling may enhance the damping of compressed silicone rubber tubes by orders of magnitude. Similar phenomena are reported by Bishop et al. [34] and Cui and Harne [22], where applying external constraint to elastomeric metamaterials leads to a growth of damping capacity.

The agreement between experimental and analytical results is not complete in Fig. 3 due to the utilization of a phenomenological model. For instance, the detailed geometry of the adaptive Helmholtz resonator and the compliance of the walls of the resonator are not taken into consideration. Yet, the salient physics observed in the experiment is reproduced through the analytical model trends. This indicates that the phenomenological model leveraged in this study is able to provide insight into the acoustic-structure influences that manifest in the enclosure-resonator system.

Overall, the experiments and analysis indicate that tuning the compression constraint applied to the resonator enhances acoustic-structure interaction via the buckling condition of the flexible member, and the acoustic damping characteristics of the resonator are likewise tuned. Scrutinizing the non-dimensional governing equation of motion helps to illuminate the influence of system parameters to realize such adaptable acoustic damping. For instance, for the compression constraint to be effective, the ratio of resonator secondary cavity stiffness to flexible member elastic stiffness, $\alpha = k_2/k_e$, should be on the same order as the load parameter p. When α is much greater than p, the flexible member is effectively fixed by a stiff acoustic spring in the secondary cavity, thus the compression constraint is unable to buckle the flexible member. If $\alpha = 0$, the flexible member interfaces with the surrounding air, thus the buckling condition of the flexible member is tuned solely by the compression constraint, and sound radiation to the environment by the vibration of the flexible member may occur.

5.2 Resonant Behavior of the Adaptive Helmholtz Resonator with Constrained Flexible Member. The transfer function of the acoustic pressure inside the resonator primary cavity to the acoustic pressure inside the enclosure cavity is investigated to gain insight on the inner-workings of the resonator under various compression conditions. The transfer function is the ratio of frequency responses of microphone M2 to that of microphone M1 in Fig. 1(*d*). In Fig. 4, experimental (*a*) and analytical (*b*) results of the transfer function phases Φ for the same experimental and analytical conditions presented in Figs. 3(*c*) and 3(*f*), respectively. The greater attenuation of the enclosure SPL occurs when the transfer function phase is nearest to −90 deg, which agrees with the results reported by Zhao et al. [35].

The compression constraint is seen through the measurements and predictions to influence the transfer function phase. Figure 4(*a*) reveals that from 0% to 4.00% to 5.78% pre-strains, the phase of the transfer function shifts to lower frequency referencing the −90 deg phase shift. In the analytical predictions in Fig. 4(*b*), a similar, albeit not as dramatic, frequency shift of the phase occurs. Although experimental results present a more dramatic shift in frequency under constraints than analytical results, utilizing the phenomenological model reveals comparable insight on the basic physics of the problem. The qualitative agreement between experimental and analytical results provides validation to the analytical model formulation and solution approach. To more deeply investigate the intricate acoustic-structure interaction phenomena observed by the adaptive resonator with internal flexible structural members, detailed parameter studies are then undertaken.

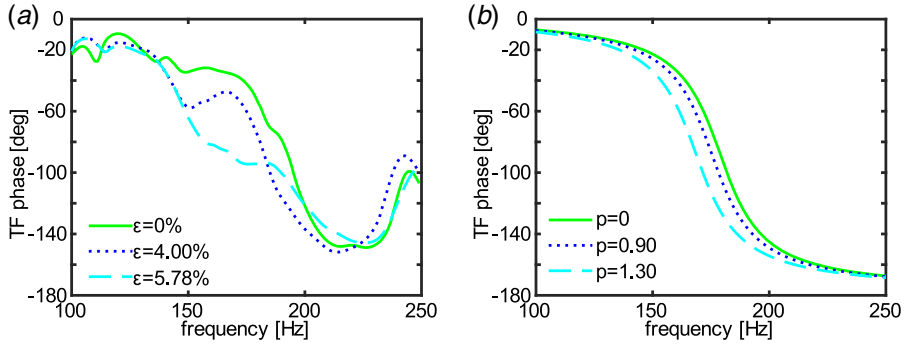

Fig. 4 Experimental results of the transfer function phase (*a*) for the same experimental set presented in Fig. 3(c). The pre-strains are indicated in the legends. Analytical results of the transfer function phase (*b*) for the same parameter set presented in Fig. 3(*f*). The compressed conditions are indicated in the legends.

6 Analytical Study of Acoustic-Structure Interaction Phenomena

6.1 Assessment of Resonator Design and Compression Extent. To broaden the understanding of methods to exploit the design and compression constraint of the resonator for adaptive control over the acoustic field in the enclosure, additional investigations are carried out. In Fig. 5 are results for the enclosure SPL as functions of the excitation frequency and load parameter. The shading indicates the SPL value. Darker shading increments indicate a 2 dB increase from the prior shading. For Fig. 5, the top thin contour plots are the results of the enclosure SPL without the resonator (the *baseline*), while the larger contour plots in Fig. 5 correspond to the enclosure with the resonator. The resonant frequency of the enclosure is indicated by a thin dashed line around 164 Hz where the enclosure SPL is 101.8 dB. Several SPL values are marked on the contour plot for convenience.

In Fig. 5(*a*), the parameters listed in Table 1 are used to generate analytical model results, except for $a_1 = 3.4$ mm. For the system parameters employed, the fundamental natural frequency of the enclosure is around 164 Hz, the natural frequency of the resonator is 166 Hz, and the fundamental frequency of the flexible member is 908 Hz. The ratio of the fundamental natural frequency of the flexible member to that of the enclosure is $f_2 = 5.54$. As presented in Fig. 5(*a*), when the load parameter p is close to zero, or large such as $p = 3$, around 9 dB attenuation of the enclosure SPL is achieved at 164 Hz. When $p = 1.75$, which is the critical load parameter value p^* calculated from Eq. (12), the enclosure indeed has a resonant peak at 164 Hz despite containing the adaptive resonator. In this latter case, the SPL value is only 0.4 dB less than the baseline SPL at this frequency. In other words, for the design of the adaptive resonator used for the results in Fig. 5(*a*), compression constraints on the resonator less than or greater than the critical value provide a considerable reduction of the enclosure SPL, whereas the critically compressed resonator is not particularly effective to attenuate the SPL.

These trends distinctly contrast to the results of the system analysis using a different parameter set in Fig. 5(*b*). For results presented in Fig. 5(*b*), the parameters for the flexible member are changed to be $S_2 = 0.0016$ m^2, $V_e = 8e-5$ m^3, $\zeta = 1$, $h = 0.01$ m, $\lambda = 145.38$, and the opening radius of the resonator is $a_1 = 3.3$ mm. The remaining system parameters are those listed in Table 1. As seen in Fig. 5(*b*), the overall trends of how the enclosure SPL is influenced by the change in load parameters are unique when compared with Fig. 5(*a*). For instance, in Fig. 5(*b*), the fundamental natural frequencies of the enclosure, the resonator, and the flexible member are 164 Hz, 162 Hz, and 155 Hz, respectively. The ratio of the fundamental natural frequency of the flexible member to that of the enclosure is $f_2 = 0.95$, which compares to $f_2 = 5.54$ for Fig. 5(*a*). The influence of the load parameter on the enclosure SPL shown in Fig. 5(*b*) is evidence of more pronounced acoustic-structure coupling. For instance, for a load parameter around the critical value $p^* = 1.18$, calculated from Eq. (12), 8.7 dB attenuation is achieved at 164 Hz in Fig. 5(*b*). For lightly compressed conditions $p \approx 0.25$ or when the load parameter is slightly greater than the critical value, such as $p \approx 1.73$, the attenuation at 164 Hz is less than 2.5 dB. Yet, for still further increase in load parameter, for instance when $p = 3$, the resonator attenuates the enclosure SPL by at least 7.8 dB over the frequency range of 156–168 Hz.

In summary, small constraint or over constraint maximizes the enclosure SPL reduction for the system in Fig. 5(*a*) when the flexible member is stiffer (908 Hz). In contrast, a critical constraint or over constraint maximizes the enclosure SPL reduction for the system in Fig. 5(*b*) when the flexible member is less stiff (155 Hz). In other words, the difference in the selection of p to achieve the greatest attenuation for the flexible structures studied in Figs. 5(*a*) and 5(*b*) is governed by the flexibility of the internal structure. The ratios of the fundamental natural frequency of the flexible member to the enclosure resonant frequency in Figs. 5(*a*) and 5(*b*) are $f_2 = 5.54$ and 0.95, respectively. Based on the results of Fig. 5, the frequency ratio f_2 exerts a significant influence on the overall interaction between acoustic and elastic physics.

6.2 Structural Acoustic Response Adaptation by Varying Compression. To more closely scrutinize the acoustic-structure coupling between the enclosure and the adaptive Helmholtz resonator, results for specified load parameters selected from Fig. 5 are presented in Fig. 6. Along with the plots of enclosure SPL in Figs. 6(*a*) and 6(*d*), the transfer function amplitude (*b*,*e*) and phase (*c*,*f*) are given for deeper insight. In Figs. 6(*a*)–6(*c*) are the enclosure SPL, transfer function amplitude, and transfer function phase computed using the same parameters as used in Fig. 5(*a*) for $p = 0$ (thick solid), $p = 1.69$ (dotted), and $p = 2$ (dashed) along with the baseline (thin solid). The near-critical value $p = 1.69$ is presented instead of the critical value $p^* = 1.75$, because the critical condition exhibits a computational singularity.

In Fig. 6(*a*), the SPL resulting in near-critical compression $p = 1.69$ condition is not greatly different than the SPL in the baseline case. A study of the corresponding transfer function results in Figs. 6(*b*) and 6(*c*) explains this result. Although the near-critical compression makes the flexible member more compliant and possessed with greater damping capacity [22], the vibration of the flexible member is mostly −180 deg out-of-phase with the pressure increase and decrease in the enclosure, evidenced by the phase difference in Fig. 6(*c*). The transfer function amplitude for $p = 1.69$ has values less than 1 as shown in Fig. 6(*b*), indicating that no magnification of acoustic pressure amplitude occurs in the resonator primary cavity in this case. Magnification of response, by $H > 1$, is required

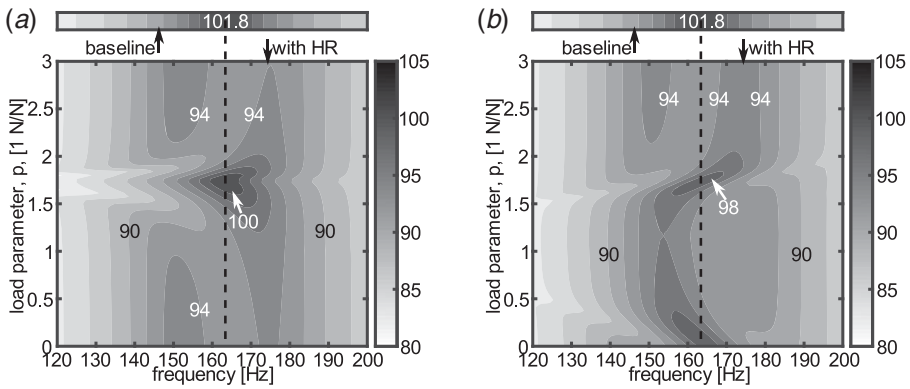

Fig. 5 Analytical results for enclosure SPL at 120–200 Hz (*x*-axis) with load parameter in the range 0–3 (*y*-axis) for a flexible member that has the fundamental natural frequency of (*a*) 908 Hz and (*b*) 155 Hz

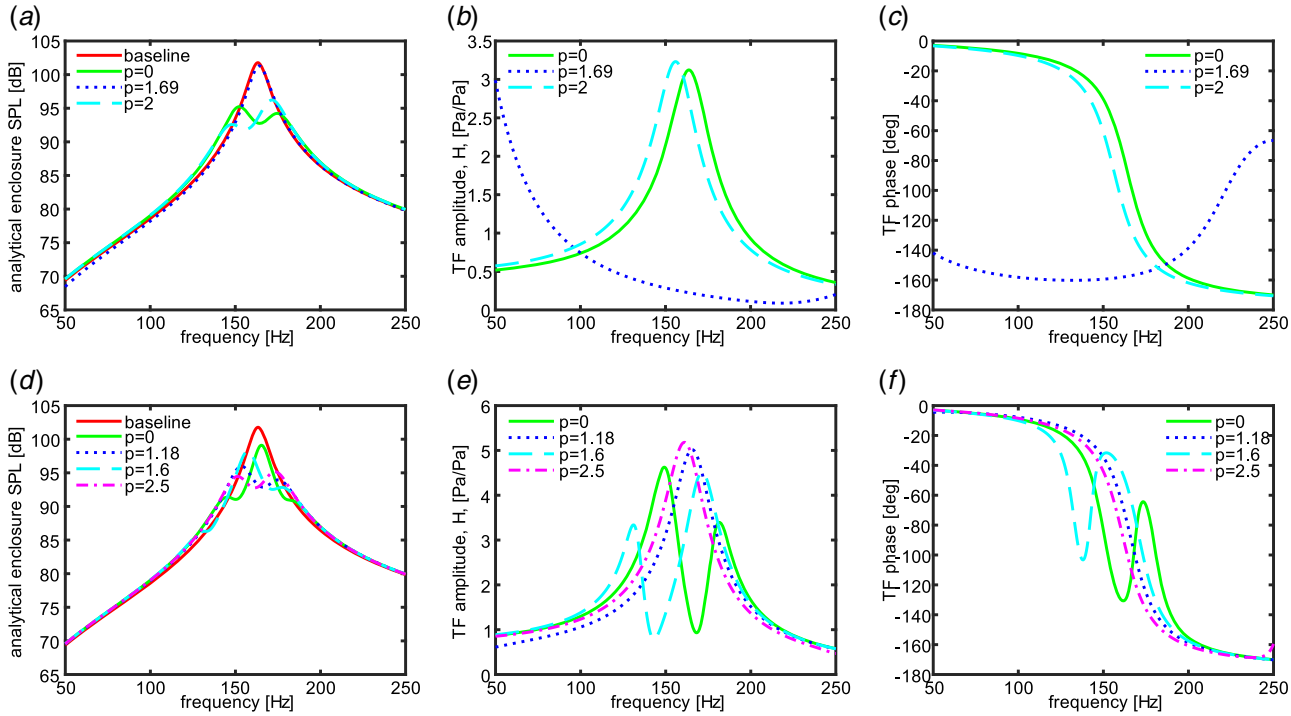

Fig. 6 Analytical results of enclosure SPL (*a*) and (*d*), transfer function amplitude (*b*) and (*e*), and transfer function phase (*c*) and (*f*) using (*a*)–(*c*) the same system parameters as in Fig. 5(*a*), and (*d*)–(*f*) the same parameters as in Fig. 5(*b*), where the baseline is indicated by thin solid curve, and load parameters are indicated in the legends

for an acoustic absorber to suppress the acoustic energy in the host enclosure.

On the other hand, when the resonator is uncompressed $p = 0$ or more highly compressed $p = 2$ than the critical value, attenuation of the enclosure SPL is achieved, as seen in Fig. 6(*a*) around the resonant frequency of 164 Hz. In Figs. 6(*b*) and 6(*c*), the transfer function amplitude and phase for the case $p = 2$ is shifted to lower frequency when compared with the uncompressed condition $p = 0$. The similar behavior of the enclosure SPL and transfer function amplitude and phase for the conditions $p = 0$ and $p = 2$ indicates similar acoustic-structure interaction in the system for the two conditions. The distinguishing factor is that in the case of $p = 2$, the flexible member is post-buckled.

The parameters used in Fig. 5(*b*) are then used to generate the results of Figs. 6(*d*)–6(*f*) where attention is given to the cases of load parameter $p = 0$ (thick solid), $p = 1.18$ (the critical value, dotted), $p = 1.6$ (dashed), and $p = 2.5$ (dash-dotted). For comparison, the baseline result is also provided in Fig. 6(*d*) (thin solid). For the uncompressed $p = 0$ condition, two peaks for the transfer function amplitude are observed in Fig. 6(*e*), and two approximately −90 deg phase shifts are evident in Fig. 6(*f*). These two frequencies around 150 Hz and 178 Hz are the same frequencies in Fig. 6(*d*) where attenuation of the enclosure SPL is most prominent for $p = 0$. On the other hand, the SPL at the enclosure resonator frequency 164 Hz is not significantly reduced. Yet, such a combination of parameters suggests that strong acoustic-structure occurs among the enclosure-resonator-flexible member system so as to give rise to two local peaks of the transfer function.

When the load parameter is at the critical point $p^* = 1.18$, a single peak appears in the transfer function amplitude around 166 Hz in Fig. 6(*e*) and one −90 deg phase shift in Fig. 6(*f*) is evident. In this event, Fig. 6(*d*) shows that the SPL for the enclosure at 164 Hz is reduced with a local minimum of around 166 Hz. If the resonator is under a constraint slightly greater than the critical load, such as $p = 1.6$ in Fig. 6(*d*), although the SPL at 164 Hz is suppressed compared with the baseline, the attenuation is not great as that achieved by the critical condition. The trends of transfer function amplitude and phase for $p = 1.6$ are similar to those for $p = 0$, although the transfer function peaks occur at distinct frequencies. Finally, when the resonator is under greater compression constraint, $p = 2.5$, as presented in Figs. 6(*d*)–6(*f*), similar behaviors compared with the critical condition are observed. The attenuation for enclosure SPL around resonance 164 Hz is achieved, and transfer function amplitude and phase have similar trend with the critical condition $p = 1.18$, albeit the features are shifted slightly to frequencies of 4 Hz lower.

Considering the collective results of Figs. 5 and 6, the acoustic-structure interaction phenomena in the system may be fully interpreted. For the specific flexible member structure studied in Figs. 5(*a*) and 6(*a*)–6(*c*) with resonant frequency 908 Hz, although the near-critical compression constraint tunes the damping of the flexible member, it does not magnify the pressure in the adaptive resonator primary cavity when compared with the enclosure cavity pressure. Only magnification of the transfer function $H > 1$ attenuates the enclosure SPL. For the flexible member structure with parameters studied in Figs. 5(*b*) and 6(*d*)–6(*f*), the natural frequency of the flexible member (155 Hz) is nearer to the natural frequency of the resonator (162 Hz) and the enclosure (164 Hz). When no compression constraint is applied ($p = 0$), a greater acoustic-structure interaction occurs due to the compatibility of stiffnesses, and two transfer function amplitude peaks and two effective attenuation frequencies are achieved. This result indicates that the resonator with the flexible member can be utilized for attenuating more than one resonance. On the other hand, once the flexible member is compressed near the critical point $p^* = 1.18$ in Fig. 6(*d*), the engagement of the flexible member is suppressed around the 164 Hz enclosure resonance. In this case, the enclosure SPL attenuation is associated more with the Helmholtz resonance of the primary resonator cavity, whereas the critically constrained member contributes additional dissipation seen by the suppressed transfer function magnitude in Fig. 6(*e*) near 164 Hz. These findings reveal insight on the interactions between acoustic and elastic physics in the adaptive resonator concept proposed here. Although this research probed the most influential parameters governing sound absorption characteristics of the tunable Helmholtz resonator, future parametric studies

may be carried out on other design details that may introduce new acoustic energy mitigating capability.

7 Conclusions

This research introduces and studies a tunable adaptive Helmholtz resonator that exploits compression upon an internal flexible structural member to tune dynamic stiffness and damping characteristics for mitigation of acoustic energy. A phenomenological analytical model is established to characterize the behavior of the resonator under compression as well as the acoustic-structure interaction inside the enclosure-resonator-flexible member system. Change of the opening radius of the resonator tunes the Helmholtz resonance and tailors acoustic-structure interaction by adjusting the significance of air impingement upon the flexible member. Larger area ratio may enhance the SPL reduction of the enclosure. Tuning the compression constraint applied to the flexible member causes a tuning on the damping effect of the resonator. Specifically, the results show that the compression constraint tunes the resonator by shifting the amplitude and phase of the transfer function of the resonator primary cavity pressure to the enclosure pressure. For a stiffer flexible member, small or large compression constraint leads to increased damping and maximum reduction of the enclosure SPL. For a softer flexible member, the resonator engages with the enclosure either like a two degrees-of-freedom sub-system or like a one degree-of-freedom system, depending on the compression constraint. Despite this broad shift of global behavior, the overall attenuation of the enclosure SPL is robust to change in compression constraint. In summary, this research uncovers fundamentals of the acoustic-structure interaction between an enclosure and a Helmholtz resonator with a compressible internal flexible member, develops an analytical tool to analyze the dynamic characteristics of this acoustic-structure system, and opens new avenues for future work on Helmholtz resonators composed of compliant materials.

Acknowledgment

This research is supported in part by the Ford Motor Company.

Appendix

The steps to solve Eqs. (4), (7), and (11) by the harmonic balance method are presented here. The non-dimensional time $\tau = \omega_0 t$ is introduced. The derivative with respect to τ is $(\mathrm{d}/\mathrm{d}\tau) = ()'$. The stiffness terms are defined by $k_0 = c^2\rho_0 S_0^2/V_0$, $k_1 = c^2\rho_0 S_1^2/V_1$, and $k_2 = c^2\rho_0 S_2^2/V_2$. Then, Eqs. (4), (7), and (11) are simplified as

$$x_0'' + \eta_0 x_0' + x_0 - \delta_1 x_1 = F_0 \cos\omega\tau \tag{A1a}$$

$$\mu_1 x_1'' + \mu_1 f_1 \eta_1 x_1' + \mu_1 f_1^2 x_1 + \delta_1^2 x_1 - \mu_1 f_1^2 \delta_2 x_e - \delta_1 x_0 = 0 \tag{A1b}$$

$$\mu_2 x_e'' + \mu_2 f_2 \eta_2 x_e' + \mu_2 f_2^2 \left(\alpha + 1 - p + \frac{\mu_1 f_1^2}{\mu_2 f_2^2}\delta_2^2\right) x_e - \mu_1 f_1^2 \delta_2 x_1 + \mu_2 f_2^2 \beta x_e^3 = 0 \tag{A1c}$$

where non-dimensional parameters are defined as $\omega = (\Omega/\omega_0)$, $\mu_1 = (m_1/m_0)$, $\mu_2 = (m_e/m_0)$, $f_1 = (\omega_1/\omega_0)$, $f_2 = (\omega_e/\omega_0)$, $\delta_1 = (S_1/S_0)$, $\delta_2 = (S_2/S_1)$, $\alpha = (k_2/k_e)$, $\beta = (k_{en}/k_e)$, $F_0 = P_0 S_0/(m_0\omega_0^2)$ and the fundamental natural frequencies are defined as $\omega_0 = \sqrt{c^2 S_0/(V_0 t_0^*)} = \sqrt{k_0/m_0}$, $\omega_1 = \sqrt{c^2 S_1/(V_1 t_1^*)} = \sqrt{k_1/m_1}$, $\omega_e = \sqrt{k_e/m_e}$.

Then, the harmonic balance method is applied to solve for x_0, x_1, and x_e. The solutions are assumed as

$$x_0(\tau) = m_0(\tau)\sin\omega\tau + n_0(\tau)\cos\omega\tau \tag{A2a}$$

$$x_1(\tau) = m_1(\tau)\sin\omega\tau + n_1(\tau)\cos\omega\tau \tag{A2b}$$

$$x_e(\tau) = g_2(\tau) + m_2(\tau)\sin\omega\tau + n_2(\tau)\cos\omega\tau \tag{A2c}$$

Then, Eqs. (A2a)–(A2c) are substituted into Eqs. (A1a)–(A1c). The coefficients in Eqs. (A2a)–(A2c) are considered to vary slowly such that the second derivatives are neglected. Higher-order harmonic terms are also neglected since only the fundamental harmonics are considered to contribute under single and low-frequency excitation. The coefficients of sine, cosine, and constant terms are then collected together to yield seven unique equations. Considering steady-state solutions, coefficients in Eq. (A2) are solved as

$$m_0 = \theta(F_0\eta_0\omega + \delta_1(1-\omega^2)m_1 + \delta_1\eta_0\omega n_1) \tag{A3a}$$

$$n_0 = \theta(F_0(1-\omega^2) - \delta_1\eta_0\omega m_1 + \delta_1(1-\omega^2)n_1) \tag{A3b}$$

$$m_1 = \phi_1\kappa + \xi\kappa m_2 + \sigma\kappa n_2 \tag{A4a}$$

$$n_1 = \phi_2\kappa - \sigma\kappa m_2 + \xi\kappa n_2 \tag{A4b}$$

where the coefficients are defined as

$$\theta = 1/(1 - 2\omega^2 + \eta_0^2\omega^2 + \omega^4)$$

$$\kappa = 1/((\delta_1^2\eta_0\theta\omega + \mu_1 f_1\eta_1\omega)^2 + (\mu_1(f_1-\omega)(f_1+\omega) + \delta_1^2(1+\theta(-1+\omega^2)))^2)$$

$$\phi_1 = F_0\delta_1\theta(-\delta_1^2\eta_0\theta - \mu_1 f_1\eta_1)\omega(-1+\omega^2) + F_0\delta_1\eta_0\theta\omega(\mu_1(f_1-\omega)(f_1+\omega) + \delta_1^2(1+\theta(-1+\omega^2)))$$

$$\xi = \mu_1 f_1^2\delta_2(\mu_1(f_1-\omega)(f_1+\omega) + \delta_1^2(1+\theta(-1+\omega^2)))$$

$$\sigma = \mu_1 f_1^2\delta_2(\delta_1^2\eta_0\theta + \mu_1 f_1\eta_1)\omega$$

$$\phi_2 = F_0\delta_1\theta(\mu_1(f_1^2 - (1+f_1^2+f_1\eta_0\eta_1)\omega^2 + \omega^4) - \delta_1^2(-1+\omega^2+\theta(1+(-2+\eta_0^2)\omega^2+\omega^4)))$$

Then, the equivalent equations

$$\Lambda m_2 - \psi n_2 = A \tag{A5a}$$

$$\psi m_2 + \Lambda n_2 = B \tag{A5b}$$

are acquired, and m_2 and n_2 are solved to be

$$m_2 = \frac{A\Lambda + B\psi}{\Lambda^2 + \psi^2} \tag{A6a}$$

$$n_2 = \frac{B\Lambda - A\psi}{\Lambda^2 + \psi^2} \tag{A6b}$$

with coefficients

$$\Lambda = \mu_1 f_1^2\delta_2^2 - \mu_1 f_1^2\delta_2\kappa\xi + \mu_2 f_2^2(\alpha+1-p) - \mu_2\omega^2 + 3\mu_2 f_2^2\beta g_2^2 + \frac{3}{4}\mu_2 f_2^2\beta r^2$$

$$\psi = \mu_1 f_1^2\delta_2\sigma\kappa + \mu_2 f_2\eta_2\omega, \quad A = \mu_1 f_1^2\delta_2\kappa\phi_1, \quad B = \mu_1 f_1^2\delta_2\kappa\phi_2$$

For Eqs. (A5a) and (A5b), the square of each equation is taken and summed to yield

$$(\Lambda^2 + \psi^2)r^2 = A^2 + B^2 \tag{A7}$$

where $r^2 = m_2^2 + n_2^2$ is the amplitude square of the response of x_e.

For steady-state solutions, one gets the equation

$$g_2\left(\mu_1 f_1^2\delta_2^2 + \mu_2 f_2^2(\alpha+1-p) + \frac{3}{2}\mu_2 f_2^2\beta r^2 + \mu_2 f_2^2\beta g_2^2\right) = 0 \tag{A8}$$

The solutions to g_2^2 are either $g_2^2 = 0$ for the symmetric solution where the equilibrium is $x_e^* = 0$, or $g_2^2 = -\mu_1 f_1^2\delta_2^2/(\mu_2 f_2^2\beta) -$

$((\alpha+1-p)/\beta)-(3/2)r^2$ for the asymmetric solution with equilibrium $x_e^*=\sqrt{-\mu_1 f_1^2\delta_2^2/(\mu_2 f_2^2\beta)-((\alpha+1-p)/\beta)}$. Then, from Eq. (A7), third-order polynomials in terms of r^2 are obtained. For $g_2^2=0$ and $g_2^2=-\mu_1 f_1^2\delta_2^2/(\mu_2 f_2^2\beta)-((\alpha+1-p)/\beta)-(3/2)r^2$, respectively, the polynomials are

$$\frac{9}{16}\mu_2^2 f_2^4\beta^2 r^6+\left[\frac{3}{2}\mu_2 f_2^2\beta(\mu_1 f_1^2\delta_2(\delta_2-\kappa\xi)+\mu_2(f_2^2(\alpha+1-p)-\omega^2))\right]r^4+\left[\psi^2+(\mu_1 f_1^2\delta_2(\delta_2-\kappa\xi)+\mu_2(f_2^2(\alpha+1-p)-\omega^2))^2\right]r^2-(A^2+B^2)=0 \tag{A9}$$

$$\frac{225}{16}\mu_2^2 f_2^4\beta^2 r^6+\left[\frac{15}{2}\mu_2 f_2^2\beta(\mu_1 f_1^2\delta_2(2\delta_2+\kappa\xi)+\mu_2(2f_2^2(\alpha+1-p)+\omega^2))\right]r^4+\left[\psi^2+(\mu_1 f_1^2\delta_2(2\delta_2+\kappa\xi)+\mu_2(2f_2^2(\alpha+1-p)+\omega^2))^2\right]r^2-(A^2+B^2)=0 \tag{A10}$$

Then, the roots for r^2 are solved from (A9) and (A10), and the corresponding solutions to x_0, x_1, and x_e are acquired through the relationships in Eqs. (A3), (A4), and (A6). The stability of each root is determined using the Jacobian. Only positive real roots r from (A9) and (A10) are meaningful. If the eigenvalues of the Jacobian have negative/positive real components, then the corresponding roots are stable/unstable. For the analytical results reported in this research, stable solutions are presented unless specified.

After acquiring the solutions to Eqs. (A2*a*)–(A2*c*), the SPL of the enclosure at each frequency is obtained

$$SPL_0=20\log_{10}\left|i\omega\rho_0 c\sqrt{m_0^2+n_0^2}/\sqrt{2}/(20\times10^{-6})\right| \tag{A11}$$

The transfer function of the acoustic pressure inside the resonator primary cavity to the acoustic pressure inside the enclosure cavity is determined in terms of amplitude H and phase Φ

$$H=\left|\left(\frac{S_1}{S_2}\sqrt{m_1^2+n_1^2}\right)/\left(\frac{S_0}{S_0^*}\sqrt{m_0^2+n_0^2}\right)\right|,\qquad \Phi=\tan^{-1}(m_0/n_0)-\tan^{-1}(m_1/n_1) \tag{A12}$$

where $S_0^*=0.0645\,\mathrm{m}^2$ is the cross-sectional area of the enclosure cavity.

References

[1] Kinsler, L. E., Frey, A. R., Coppens, A. B., and Sanders, J. V., 2000, *Fundamentals of Acoustics*, John Wiley and Sons, New York.
[2] Blackstock, D. T., 2000, *Fundamentals of Physical Acoustics*, Wiley, New York.
[3] Nudehi, S. S., Duncan, G. S., and Farooq, U., 2013, "Modeling and Experimental Investigation of a Helmholtz Resonator With a Flexible Plate," ASME J. Vib. Acoust., **135**(4), p. 041102.
[4] Sanada, A., and Tanaka, N., 2013, "Extension of the Frequency Range of Resonant Sound Absorbers Using Two-Degree-of-Freedom Helmholtz-Based Resonators With a Flexible Panel," Appl. Acoust., **74**(4), pp. 509–516.
[5] Zhang, H., Wei, Z., Zhang, X., Fan, L., Qu, J., and Zhang, S., 2017, "Tunable Acoustic Filters Assisted by Coupling Vibrations of a Flexible Helmholtz Resonator and a Waveguide," Appl. Phys. Lett., **110**(17).
[6] Park, C. M., Park, J. J., Lee, S. H., Seo, Y. M., Kim, C. K., and Lee, S. H., 2011, "Amplification of Acoustic Evanescent Waves Using Metamaterial Slabs," Phys. Rev. Lett., **107**(19).
[7] Lee, S. H., Park, C. M., Seo, Y. M., Wang, Z. G., and Kim, C. K., 2010, "Composite Acoustic Medium With Simultaneously Negative Density and Modulus," Phys. Rev. Lett., **104**(5), p. 054301.
[8] Kurdi, M., Nudehi, S., and Duncan, G. S., 2019, "Tailoring Plate Thickness of a Helmholtz Resonator for Improved Sound Attenuation," ASME J. Vib. Acoust., **141**(3), p. 034502.
[9] Gourdon, E., Savadkoohi, A. T., and Vargas, V. A., 2018, "Targeted Energy Transfer From One Acoustical Mode to an Helmholtz Resonator With Nonlinear Behavior," ASME J. Vib. Acoust., **140**(6), p. 061005.
[10] Tang, P. K., and Sirignano, W. A., 1973, "Theory of a Generalized Helmholtz Resonator," J. Sound Vib., **26**(2), pp. 247–262.
[11] Selamet, A., Xu, M. B., Lee, I.-J., and Huff, N. T., 2005, "Helmholtz Resonator Lined With Absorbing Material," J. Acoust. Soc. Am., **117**(2), pp. 725–733.
[12] Li, D., and Cheng, L., 2007, "Acoustically Coupled Model of an Enclosure and a Helmholtz Resonator Array," J. Sound Vib., **305**(1–2), pp. 272–288.
[13] Zhao, D., and Morgans, A. S., 2009, "Tuned Passive Control of Combustion Instabilities Using Multiple Helmholtz Resonators," J. Sound Vib., **320**(4–5), pp. 744–757.
[14] Griffin, S., Lane, S. A., and Huybrechts, S., 2001, "Coupled Helmholtz Resonators for Acoustic Attenuation," ASME J. Vib. Acoust., **123**(1), pp. 11–17.
[15] Tang, S. K., Ng, C. H., and Lam, E. Y. L., 2012, "Experimental Investigation of the Sound Absorption Performance of Compartmented Helmholtz Resonators," Appl. Acoust., **73**(9), pp. 969–976.
[16] Kurdi, M. H., Duncan, G. S., and Nudehi, S. S., 2014, "Optimal Design of a Helmholtz Resonator With a Flexible End Plate," ASME J. Vib. Acoust., **136**(3), p. 031004.
[17] Lyon, R. H., 1963, "Noise Reduction of Rectangular Enclosures With one Flexible Wall," J. Acoust. Soc. Am., **35**(11), pp. 1791–1797.
[18] Hu, N., and Burgueño, R., 2015, "Buckling-Induced Smart Applications: Recent Advances and Trends," Smart Mater. Struct., **24**(6), p. 063001.
[19] Kochmann, D. M., and Bertoldi, K., 2017, "Exploiting Microstructural Instabilities in Solids and Structures: From Metamaterials to Structural Transitions," ASME Appl. Mech. Rev., **69**(5), p. 050801.
[20] Wang, P., Casadei, F., Shan, S., Weaver, J. C., and Bertoldi, K., 2014, "Harnessing Buckling to Design Tunable Locally Resonant Acoustic Metamaterials," Phys. Rev. Lett., **113**(1), p. 014301.
[21] Nayfeh, A. H., and Mook, D. T., 1995, *Nonlinear Oscillations*, Wiley, Weinheim.
[22] Cui, S., and Harne, R. L., 2018, "Characterizing the Nonlinear Response of Elastomeric Material Systems Under Critical Point Constraints," Int. J. Solids Struct., **135**, pp. 197–207.
[23] Wang, L., and Bertoldi, K., 2012, "Mechanically Tunable Phononic Band Gaps in Three-Dimensional Periodic Elastomeric Structures," Int. J. Solids Struct., **49**(19–20), pp. 2881–2885.
[24] Pai, P. F., 2010, "Metamaterial-Based Broadband Elastic Wave Absorber," J. Intell. Mater. Syst. Struct., **21**(5), pp. 517–528.
[25] Ingard, U., 1953, "On the Theory and Design of Acoustic Resonators," J. Acoust. Soc. Am., **25**(6), pp. 1037–1061.
[26] Xu, M. B., Selamet, A., and Kim, H., 2010, "Dual Helmholtz Resonator," Appl. Acoust., **71**(9), pp. 822–829.
[27] Leissa, A. W., 1969, *Vibration of Plates*, Scientific and Technical Information Division, National Aeronautics and Space Administration, Washington, DC.
[28] Virgin, L. N., 2007, *Vibration of Axially Loaded Structures*, Cambridge University Press, Cambridge.
[29] Leissa, A. W., 1973, "The Free Vibration of Rectangular Plates," J. Sound Vib., **31**(3), pp. 257–293.
[30] Hodges, D. H., 1984, "Proper Definition of Curvature in Nonlinear Beam Kinematics," AIAA J., **22**(12), pp. 1825–1827.
[31] Harne, R. L., and Wang, K. W., 2017, *Harnessing Bistable Structural Dynamics: for Vibration Control, Energy Harvesting and Sensing*, John Wiley & Sons Ltd, Chichester.
[32] Rao, S. S., 2004, *Mechanical Vibrations*, 4th ed., Pearson Prentice Hall, Upper Saddle River, NJ.
[33] Lakes, R. S., 2001, "Extreme Damping in Compliant Composites With a Negative-Stiffness Phase," Philos. Mag. Lett., **81**(2), pp. 95–100.
[34] Bishop, J., Dai, Q., Song, Y., and Harne, R. L., 2016, "Resilience to Impact by Extreme Energy Absorption in Lightweight Material Inclusions Constrained Near a Critical Point," Adv. Eng. Mater., **18**(11), pp. 1871–1876.
[35] Zhao, D., A'Barrow, C., Morgans, A. S., and Carrotte, J., 2009, "Acoustic Damping of a Helmholtz Resonator With an Oscillating Volume," AIAA J., **47**(7), pp. 1672–1679.